Deep–Sea Research II 191-192 (2021) 104953

Contents lists available at ScienceDirect

Deep-Sea Research Part II

journal homepage: www.elsevier.com/locate/dsr2

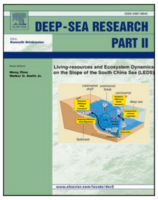

Seasonality of the Somali Current/Undercurrent system

Nan Zang[a,b,c,d], Janet Sprintall[e,*], Rémi Ienny[f], Fan Wang[a,b,c,d]

[a] CAS Key Laboratory of Ocean Circulation and Waves, Institute of Oceanology, Chinese Academy of Sciences, Qingdao, 266071, China
[b] Center for Ocean Mega-Science, Chinese Academy of Sciences, Qingdao, 266071, China
[c] Laboratory for Ocean Dynamics and Climate, Pilot National Laboratory for Marine Science and Technology (Qingdao), Qingdao, 266071, China
[d] College of Marine Science, University of Chinese Academy of Sciences, Qingdao, 266071, China
[e] Scripps Institution of Oceanography, U.C. San Diego, La Jolla, CA, 92093, USA
[f] MARAM, University of Bremen, Bremen, Germany

ARTICLE INFO

Keywords:
Somali current
Somali undercurrent
Seasonal variability
Baroclinic adjustment

ABSTRACT

The connected western boundary current system in the Arabian Sea plays an important role in the exchange of heat, mass, and freshwater and their distribution. Nonetheless, the dynamics and time scales of the processes and characteristics of this boundary current are not well understood because most prior measurements were only for a limited period or only resolved the surface circulation. Seasonality of the Somali Current (SC)/Undercurrent (SUC) system is investigated using a multi-decadal time series of ocean temperature and salinity profiles. The SC is driven principally by the seasonal monsoon winds, flowing southwestward in the winter monsoon (January–March), then reverses to northeastward in the summer monsoon (June–September). The subsurface southwestward SUC is found during the transition seasons in April–June and again in September–November. A vertical normal mode decomposition shows that the surface SC is mainly controlled by the seasonally varying first baroclinic mode and the barotropic component (a combined 86.5% of the total variance), while the SUC variations can be explained by the superimposition of the first and second baroclinic modes (a combined 75.9% of the total variance). Here we show that the occurrence of the countercurrent is not only due to the baroclinic adjustment caused by the wind forcing, but also a response to the complex salinity structure caused by the intrusion of high salinity water masses. Specifically, the presence of the salty water masses from the northern Arabian Sea during the boreal summer monsoon inhibits the southwestward flowing SUC and results in a baroclinic structure that supports a subsurface northeastward flow, aligned with the surface current. This suggests that salinity dynamics play a fundamental role in the circulation of the boundary current system of the Arabian Sea.

1. Introduction

The Somali Current (SC)/Undercurrent (SUC) is the western boundary current (WBC) system of the Arabian Sea. The SC/SUC is characterized by narrow, fast jets that exhibit considerable variability in intensity, vertical profile and width on many time scales (see Schott and McCreary, 2001, and references therein). This poses significant challenges in the estimation of the velocity and volume transport of the SC/SUC system. In addition, the SC is connected to a complex system of coastal and larger scale currents that themselves may be transient and respond to the monsoonal wind forcing.

There have been a number of studies investigating the observed near-surface circulation of the Arabian Sea WBC system although many of the observational studies are based on limited records in terms of measurement duration or else primarily focus on the use of surface measurements from drifters and altimeters (Schott and McCreary, 2001; Schott et al., 2009; Beal and Donohue, 2013; Beal et al., 2013). Before the onset of the summer monsoon (March–May), the SC flows northward as an extension of the East African Coastal Current arising from the south at 3–4°N (Schott and McCreary, 2001; Beal et al., 2013). During the boreal summer monsoon (June–September), the northeastward flowing SC grows rapidly to an annual maximum velocity. An eddy-type feature known as the Great Whirl (GW) can appear as early as April but seems to strengthen rapidly during the summer monsoon and typically dissipates in early November (Schott et al., 1997, 2009; Schott and McCreary, 2001; Beal and Donohue, 2013; Vic et al., 2014; Wirth et al., 2002).

---

* Corresponding author.
E-mail address: jsprintall@ucsd.edu (J. Sprintall).

https://doi.org/10.1016/j.dsr2.2021.104953
Received 4 February 2020; Received in revised form 13 July 2021; Accepted 1 August 2021

These studies suggest that the GW appears to be controlled by a combination of local wind forcing, Rossby wave dynamics and internal instabilities. The SC reverses to be southwestward during the boreal winter monsoon (December–February) (Donguy and Meyers, 1995).

Little is known about the subsurface circulation in the Arabian Sea primarily because there have been so few long-term observational subsurface records. Quadfasel and Schott (1983) found a southwestward-flowing SUC at ~150–600 m depth beneath the seasonally reversing SC using a 2.5-year time series from moorings on the continental slope off Somalia near 5°N. A shorter moored time series observed a deeper southwestward SUC at 700–800 m during the winter monsoon that was clearly marked by Red Sea Water (RSW) (Schott and Fisher, 2000). From March to May, the SUC flowed southwestward opposing the northeastward flowing SC. After the summer monsoon onset in June–July, Quadfasel and Schott (1983) suggested that the SUC is destroyed when the deep-reaching northern Somali Gyre spins up in a barotropic mode. The southeastward SUC appears to reestablish in August after the gyre system breaks down remaining in opposition to the northward SC until the return to southward surface flow at the onset of the winter monsoon around November. Thus, the observations suggested the SUC is highly variable in time and both vertical and horizontal space.

Direct measurements of the volume transports within the SC/SUC range from 5 to 10 Sv during the winter monsoon when the flow is mostly surface-trapped and probably mostly Ekman-driven (Hastenrath and Greischar, 1991; Beal et al., 2013) to 25–35 Sv during the summer monsoon when the current system can extend to ~2000 m depth, albeit this transport estimate was obtained from a single hydrographic section (Beal and Chereskin, 2003). How these volume transports in the SC and the SUC change in both pathway and strength over the evolution of the monsoons is still relatively poorly understood (Luther, 1999; Wirth et al., 2002; Beal and Donohue, 2013).

Thus, despite some recent progress in understanding the SC/SUC phenomenology, because of the sparse number of observations, the mechanisms responsible for the spatial structure, strength and variability of the Arabian Sea boundary current circulation remain largely unclear. Early studies suggested the initial development of the Arabian Sea WBC system during the summer monsoon was due to remote wind forcing that sets up a Sverdrupian response. Local wind stress then established and sustained the SC throughout the remaining monsoon period (Lighthill, 1969; Cane and Gent, 1984; Philander and Pacanowski, 1981; McCreary and Kundu, 1988). However recent analysis of drifter and satellite data suggests that the initial reversal within the surface layer, that occurs well before the onset of the summer monsoon, could be in response to the arrival of annual Rossby waves that radiate from the southern tip of India (Brandt et al., 2002; Beal and Donohue, 2013). On the other hand, local wind variability and boundary current detachment/instability have also been suggested as playing a major role in setting up the SC (Schott and McCreary, 2001). Unquestionably the semi-annual monsoon winds strongly influence the strength, direction and variability of the near-surface currents and semi-permanent eddies of the boundary current during their peak phase. It is also worth explicitly pointing out that both the phase and strength of the monsoon vary from year to year and this will rectify the seasonal and intra-seasonal variability in a way that is not well understood at present (Schott et al., 1997).

Some limited modelling studies have shown similar features to those observed by the sparse number of subsurface measurements and have suggested the reason for the presence of the SUC (McCreary and Kundu, 1985; McCreary et al., 1993). Jensen (1991) used a reduced-gravity model that showed that the disappearance of the SUC in the boreal spring is partly due to the arrival of deep equatorial undercurrents, while the regeneration of the SUC in the fall is associated with the decay of the GW and reversal of the equatorial currents. Using a 2.5-layer model, McCreary et al. (1993) studied the Indian Ocean circulation and suggested that the southwestward SUC occurred from October through February resulting in part from forcing during the previous Southwest Monsoon. From March through May the SUC is thought to be generated by the propagation of a Rossby wave from the west coast of India (McCreary et al., 1993; Visbeck and Schott, 1992). Nonetheless, given the relatively short observational subsurface records, it remains unclear whether the SUC is a persistent feature of the monsoon circulation in the Arabian Sea and over what depth ranges. Clearly the complex balance between the local and remote wind forcing, the complex circulation and the role they play in the evolution of the SC/SUC system deserves further attention.

This study combines complementary multi-decadal *in situ* datasets to investigate the seasonality of the surface and subsurface SC/SUC system and explore the likely mechanisms responsible for that variability. A 30-year record of geostrophic velocity across this western boundary current is constructed from year-round, frequently-repeated XBT measurements along with more recent Argo profiles. The unprecedented length of the observational time series allows for a more robust picture of the seasonal circulation in the Arabian Sea western boundary currents than the previously limited records have permitted. The paper is organized as follows. Section 2 introduces the data sets and methods used in our study. Section 3 describes the seasonal variability of the SC/SUC. Section 4 analyses the dynamics responsible for the seasonal variability. Section 5 is the summary and conclusion.

2. Data and methodology

2.1. Temperature and salinity profiles and remotely sensed data

This project makes use of historical eXpendable Bathy Thermograph (XBT) temperature profiles for calculations of geostrophic shear in the upper 750 m of the Arabian Sea boundary current. Specifically, we use XBT data from the designated transect IX12 that runs from Fremantle, Western Australia to the Red Sea (Fig. 1). IX12 has been occupied since 1986 and is repeated 7–26 times a year with XBTs deployed from volunteer merchant container vessels. There has been a total of 388 transects from 1986 to 2003 (Fig. 1c). Temperature profiles with 0.7 m vertical resolution over the upper 750 m are obtained approximately every 25 km, which gives a sufficiently high spatial resolution to resolve the subsurface spatial structure of mesoscale eddies and the boundary currents. The XBT probes have an accuracy of 0.15 °C. Systematic errors in fall-rate equations of the XBTs were corrected following Hanawa et al. (1995) and Wijffels et al. (2008), with additional checks provided by inter-comparisons of temperature-depth profiles from nearest XBT neighbors (Bailey et al., 1994).

Because of inclement weather and currents, the ship tracks may not always be exactly repeating. Furthermore, the ship tracks also changed towards the end of the record due to the increased risk associated with piracy along the Somalia coast. Consequently, there are three preferred vessel transects (Fig. 1a). For this study, we use the XBT profiles from transect-1 that crosses the boundary current from 57°E to the coastline at 51.5°E. This portion of the transect is roughly 680 km long and so takes a little under one day to transit at ship speeds of 20 knots. Thus, each XBT transect can be thought of as being somewhat synoptic especially given the monthly time scales of interest in this study. Transect-1 was occupied 265 times, with roughly 120–240 profiles per month (Fig. 1d) for determining the seasonal cycle.

The monthly gridded Argo product is derived from individual Argo temperature and salinity profiles from 2004 to 2018 (Roemmich and Gilson, 2009). The spatial resolution of the gridded Argo data is 1 ° × 1 ° and there are 58 standard pressure levels spanning 0–2000 db. In our study, the gridded Argo product is used to provide the salinity field in the upper 2000 db as well as the deeper temperature profile from 750 to 2000 db. The gridded Argo product uses a weighted least-squares fit to the nearest 100 Argo profiles within a given month so that even grid points that lie in depths that are less than 2000 db (the typical Argo profile depth) are resolved (Roemmich and Gilson, 2009). Nonetheless,

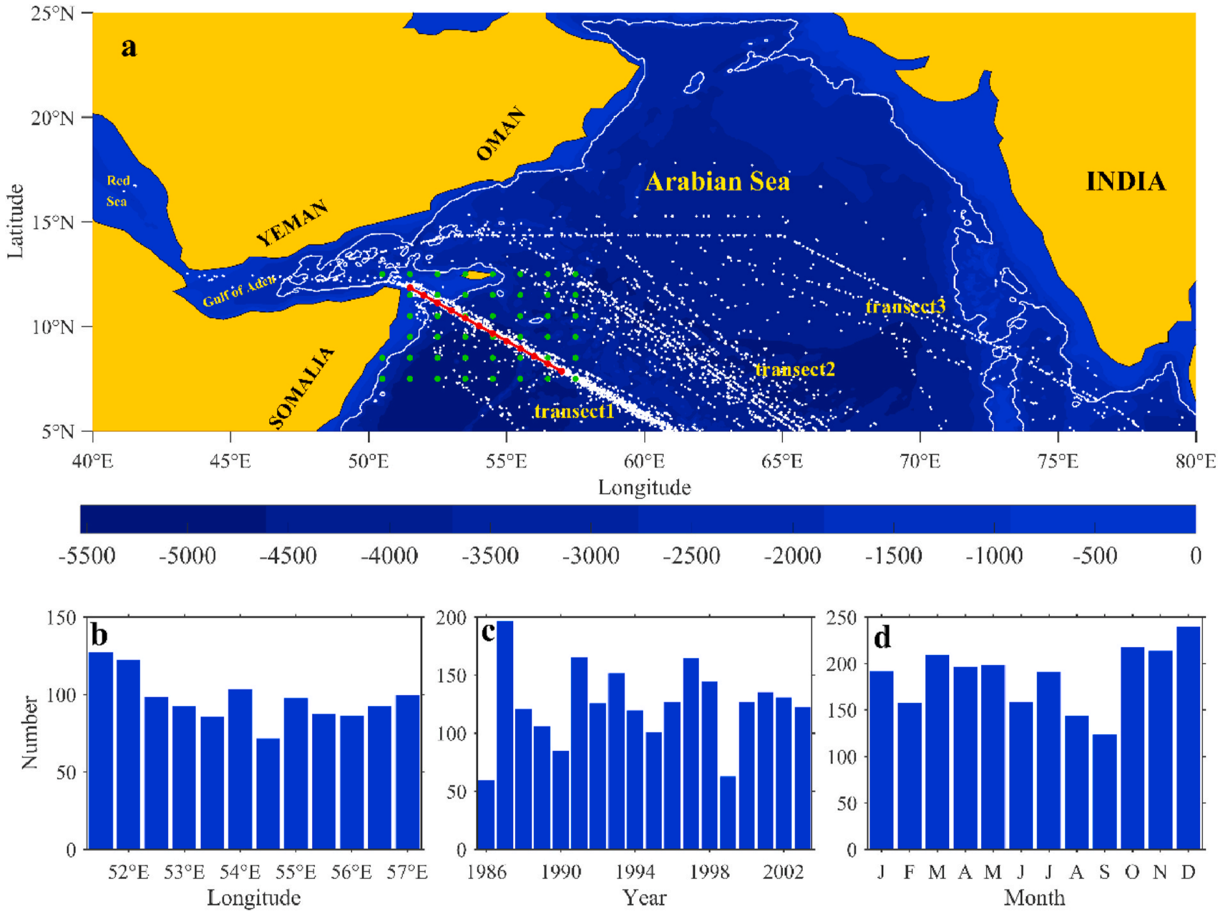

Fig. 1. (a) Distribution of XBT profiles (white dots) in the Arabian Sea, red dots represent the nominal position of Transect-1 used in the study, and gridded Argo points (green dots). The thin white line is the 2000 m isobath. Number of XBT profiles with (b) longitude, and the (c) annual and (d) monthly distribution of XBT profiles used to construct the temperature (0–750 m) along Transect-1.

the number of Argo profiles is very limited near the Somali coastline boundary (not shown) where there are many more XBT profiles (Fig. 1b). Hence, the higher-resolution XBT temperature data are not only useful for filling the upper 0–750 db but are crucial to fill the near coastal area inshore of the 2000 isobath where fewer Argo measurements are available.

Two remotely sensed products are used in our analysis. The monthly mean absolute dynamic topography (ADT) product from the Archiving, Validation, and Interpretation of Satellite Oceanographic (AVISO) from the period 1993–2017 provides a regional view of the derived mean geostrophic velocity. The wind velocity is from the Cross-Calibrated Multi-Platform (CCMP) Level 3.5a over the period of 1987–2011. The horizontal resolution of the gridded ADT and wind velocity data products is 0.25 ° × 0.25 °.

2.2. Gridded fields

To obtain the monthly temperature and salinity sections along the transect, we first grid the XBT (temperature from 0 to 750 db) data by averaging the monthly data within a 0.62° along-track by 0.5° across-track bin. The values were assigned to the along-track center of each bin (red dots in Fig. 1). We then interpolated the monthly temperature (750–2000 db) and salinity (0–2000 db) from the Argo gridded data (green points in Fig. 1) into the same bin center as the XBT data using a distance-weighted linear interpolation of the four closest Argo grid points. The monthly temperature and salinity fields constructed at each point along the transect are then interpolated to a 10 db vertical spacing. To combine each monthly XBT (0–750 db) and Argo (750–2000 db) temperature field, and eliminate the climatological differences between the XBT (1986–2003) and Argo (2004–2018) data, we obtain the monthly temperature anomalies:

$$T'_{Argo} = T_{Argo} - \overline{T_{Argo}} \tag{1}$$

$$T'_{XBT} = T_{XBT} - \overline{T_{XBT}} \tag{2}$$

where T_{Argo} and T_{XBT} are the temperature section from Argo and XBT for each month, $\overline{T_{Argo}}$ and $\overline{T_{XBT}}$ are the record length mean temperature, and T'_{Argo} and T'_{XBT} are the resulting anomalies for each month. Once we obtain the anomalies, we combine the T'_{XBT} above 750 db with the T'_{Argo} below 750 db and obtain the complete monthly temperature section by adding back the long-term full depth (0–2000 db) temperature mean constructed from the Argo temperature field.

The constructed monthly mean temperature and salinity sections were used to calculate the monthly mean geostrophic currents and the volume transport across the section. We calculated the geostrophic currents by estimating the dynamic height (D) which is the vertical integration of the specific volume anomaly (ε):

$$\mathrm{V} = \frac{1}{fL}(D_2 - D_1) = \frac{1}{fL}\int_{p_{ref}}^{p}(\varepsilon_2 - \varepsilon_1)dp, \tag{3}$$

where f is the Coriolis parameter, L is the distance between the adjacent grid points, p is pressure, p_{ref} is pressure of the reference level (2000 db), D_1 and D_2 are the dynamic height and ε_1 and ε_2 are the specific volume anomalies at adjacent grid points along the section. We chose 2000 dbar as the reference level because the currents at that depth are very weak: mooring records showed the velocity at 2000 m is near zero along the Somalia coast (Schott and Fisher, 2000; Schott and McCreary, 2001; Reppin et al., 1999). Similarly, Vic et al. (2014) calculated the kinetic energy at 2000 m depth using ROMS model output and showed that the kinetic energy at 2000 m is only about 1% of that at the surface.

Definitions used for integrated transport calculations in the SC/SUC system vary from study to study and no consistent method or integration range (pressure/depth/density surfaces and horizontal along-track range) has as yet emerged (see for example Donguy and Meyers, 1995; Schott and Fisher, 2000; Beal and Chereskin, 2003 that all used different computational ranges). We explored various options for the transport integration limits, as well as totaling together only those flows that were positive or negative along the section. However, these techniques never adequately or consistently resolved the variable SUC and SC that are

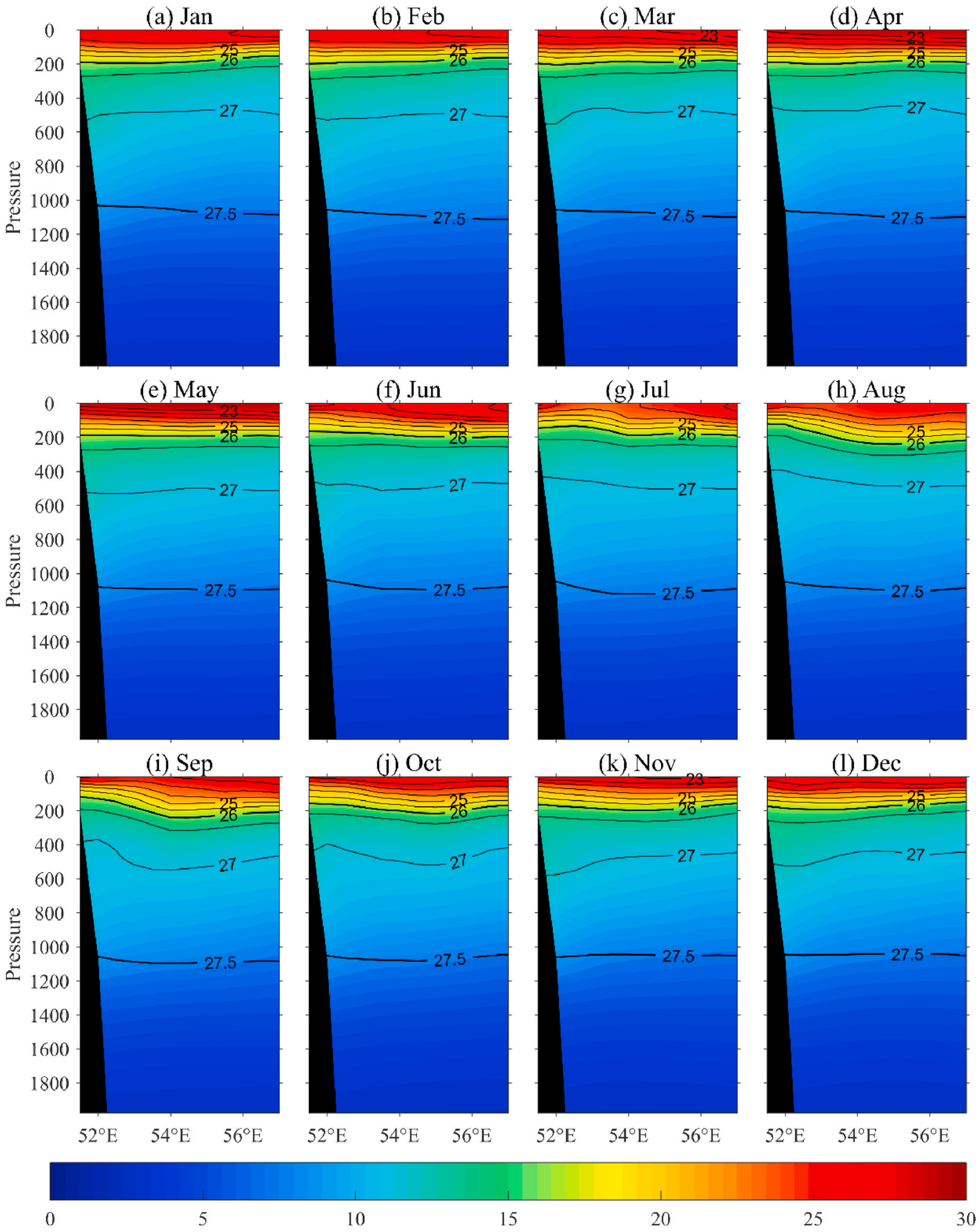

Fig. 2. Monthly temperature (unit: °C) structure along the transect shown in Fig. 1. Black solid lines are the potential density isopycnals at 0.5 kg m^{-3} intervals.

evident in the along-track velocity sections (see Section 3). Hence, in our study we have taken the approach to calculate the integrated transport from geostrophic currents referenced to 2000 db (equation (3)) from the surface to 1975 db and between 51.5°E–54°E along transect-1 (Fig. 1). Thus, while we do not perfectly capture all the transport variability in the individual discrete SC and SUC that vary in both depth range and horizontal extent, our calculations are at least self-consistent from month to month.

2.3. Vertical mode decomposition

To better assess what drives the vertical structure of velocity in the western boundary current and whether this can be explained through linear theory we perform a vertical normal mode decomposition (see

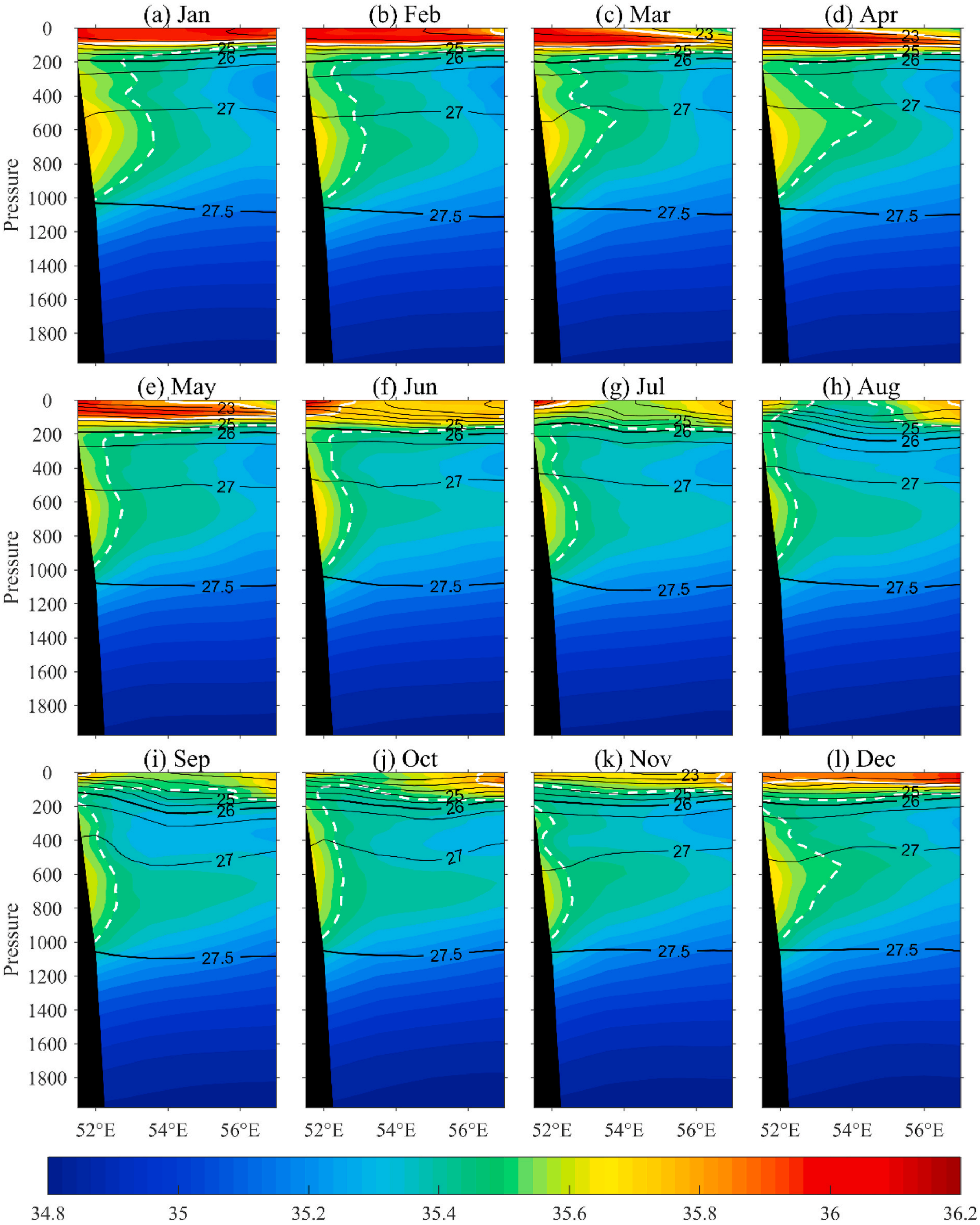

Fig. 3. Monthly salinity along the transect shown in Fig. 1. White solid lines and dotted lines are the 35.8 and 35.5 isohalines representing ASHSW and RSW, respectively. Black lines are the potential density isopycnals at 0.5 kg m^{-3} intervals.

Thompson and Emery, 2014). The vertical modes can be expressed as the eigenfunctions $\phi_n(z)$ that satisfy:

$$\left(\frac{1}{N_s^2}\phi_{nz}\right)_z = -\frac{1}{c_n^2}\phi_n(z),\ n = 0, 1, 2, \ldots..,\tag{4}$$

where N_s^2 is the squared Brunt-Väisälä frequency, $\phi_{nz} = \frac{\partial\phi_n(z)}{\partial z}$ is the vertical derivative of the nth vertical structure function, and c_n is the eigenvalue. The n = 0 eigenfunction represents the barotropic mode of the system, and for n ≥ 1, the nth eigenfunction represents the nth baroclinic mode. Geostrophic velocity can then be projected onto each normalized vertical normal mode function $\phi_n(z)$,

$$T^n(t) = \frac{\langle V(z,t)\cdot\phi_n(z)\rangle}{\sqrt{\phi_n(z)\cdot\phi_n(z)}},\tag{5}$$

$$V^n(z,t) = \phi_n(z) \times T^n(t),\tag{6}$$

where $T^n(t)$ is the projection coefficient and $V^n(z,t)$ is the velocity of the *n*th baroclinic mode.

3. Seasonal variability of the Somali Current/Undercurrent

The monthly temperature and monthly salinity along the section reconstructed from XBT and Argo data are shown in Figs. 2 and 3 respectively, with potential density contour overlain. A relatively warm (>26 °C) surface layer exists year-round (Fig. 2). From December to May the slope of the shallow isotherms is relatively flat (Fig. 2l, a-e). From June to November the isotherms in the upper layer shoal toward the coastline likely in response to the upwelling driven by the northeastward wind (Fig. 2f–k). The high salinity water mass above $\sigma_0 = 26$ kg m^{-3} is the Arabian Sea High Salinity Water (ASHSW, shown where S > 35.8 psμ in Fig. 3). ASHSW forms in the northern Arabian Sea during boreal winter due to excess evaporation and then spreads southward (Kumar and Prasad, 1999; Prasad and Ikeda, 2002; Joseph, 2005). During December–March (Fig. 3l, a-c), the high salinity core extends into the western coastal boundary as the flow is predominantly zonal from the east to west, then bifurcates into northward and southward flows at the coast (Kumar et al., 1999). During April and May, the northeast winds become weak and the core of ASHSW begins to move eastward (Fig. 3d and e). The onset of southwest winds along the western boundary during late May and early June results in an offshore Ekman transport, leading to coastal upwelling that pushes the ASHSW offshore (Fig. 3f). During July to November when the stronger southwest monsoon reverses the regional ocean circulation, an eastward zonal current further advects the high salinity core of ASHSW eastward (Fig. 3g–k).

Below the 26 kg m^{-3} isopycnal, the vertical structure of the water column is quite complex and heavily influenced by the salinity structure. From June to November the isotherms deepen toward the shore, while the isopycnals shoal (Fig. 2f–k). This occurs in response to the intrusion of warm and salty water along the western boundary. This high salinity water mass centered about 600 dbar is the Red Sea Water (RSW, where S > 35.5 psμ between $\sigma_0 = 26$ kg m^{-3} and $\sigma_0 = 27.5$ kg m^{-3}). RSW flows out of the Red Sea through the Strait of Bab el Mandeb and spreads into the Arabian Sea (Sharpiro and Meschanov, 1991). The spreading of RSW has monsoonal variability and extends further offshore along the Somali coast during the winter monsoon (December–April) (Fig. 3l, a-d). The transition region at ~200–400 dbar (Fig. 3) between the surface ASHSW and the deeper RSW might be the Persian Gulf Water (PGW). PGW forms in the Persian Gulf and flows into the Gulf of Oman then sinks to depths between 200 and 250 m (Kumar and Prasad, 1999). Kumar and Prasad (1999) summarized the characteristics of PGW in the Arabian Sea as having temperature of 13–19 °C and salinity of 35.1–37.9. During the boreal winter monsoon, there is southward spreading of PGW along the western boundary, which potentially might mix with the RSW. During the summer monsoon, the presence of PGW is more diffused because of the effect of the Findlater Jet (Prasad et al., 2001). The seasonal variations in the high salinity ASHSW and RSW water masses change the baroclinic structure along the coast, and in Section 4 we will show that this leads to changes in the geostrophic currents.

The ASHSW and RSW are also clearly evident in the T-S diagram (Fig. 4a). The core salinity of ASHSW is > 35.8 psμ between potential densities $22.5 < \sigma_0 < 24.5$ kg m^{-3} while the core salinity of RSW is > 35.5 psμ between $26.5 < \sigma_0 < 27.5$ kg m^{-3}. (Note that there is no obvious salinity maximum between $24.5 < \sigma_0 < 26.5$ kg m^{-3} that might indicate an admixture of PGW and RSW). Using these definitions, we calculated the monthly mean salinity content (psu m^2) of RSW and ASHSW along the transect from 51.5°E–54°E (Fig. 4b and c). The monthly mean salinity content of both ASHSW and RSW have an annual cycle dominated by the monsoon reversals with inventories that are higher in winter and lower in summer (Kumar and Prasad, 1999; Schott and McCreary, 2001; Prasad and Ikeda, 2002; Joseph, 2005; Beal et al., 2000). The RSW cycle is also influenced by the exchange of flow between the Red Sea and the Arabian Sea. Murray and Johns (1997) found the transport through Bab El Mandeb is higher in boreal winter compared to summer. In winter, the high salinity RSW is formed in the northern part of the Red Sea when strong evaporation leads to denser water that sinks. The high salinity water is then transported as part of the deep outflow into the Gulf of Aden (Murray and Johns, 1997). In summer, the along strait flow is a 3-layer structure with a weak deep outflow, a thick intermediate inflow layer of cold low salinity water from the Gulf of Aden, and outflow in the near surface layer. The reduced deep outflow results from the cessation of deep-water formation in late spring, while the surface outflow is attributed to the seasonal wind reversal during the summer monsoon (Murray and Johns, 1997). The seasonality of the export of the RSW into the northern Arabian Sea (Murray and Johns, 1997) thus corresponds well with the inventory of RSW observed across the transect-1 section (Fig. 4b) appearing slightly later reflecting a reasonable advective time scale of ~1 month.

The monthly geostrophic velocity calculated from the temperature (Fig. 2) and salinity (Fig. 3) fields is shown in Fig. 5. During the boreal winter monsoon period (December–March, Fig. 5l, a-c) the main core of the surface SC flows southwestward across the section. In December there is a hint of northeastward flow inshore across the continental slope (Fig. 5l). As noted above, during winter there is flow from the east between 9° and 11°N at the northern end of the transect that then bifurcates at the coast to flow northeastward and southwestward (Jensen, 1991; Kumar, 1999; Schott and Fisher, 2000; Schott et al., 2001) and this inshore flow may be a manifestation of that northward branch. In the April–May transition period, the southwestward flow weakens and some weak northeastward flow is evident in the upper ocean near the coastline (Fig. 5d and e). This may be related to the incoming annual Rossby waves (McCreary et al., 1993). Beneath the northeastward surface layer flow, an opposing subsurface equatorward flow is found at ~200–500 db with a core velocity of ~2.5 cm/s in April that shoals and extends further offshore with a core velocity of ~4 cm/s in May. The southwestward undercurrent gradually weakens and narrows in June when the surface northeastward flow begins to strengthen due to reversals in the monsoon wind and the appearance of the GW (Fig. 5f). The anti-cyclonic GW, manifested as northeastward flow from 52° to 54°N and southwestward flow offshore of this, is hinted at in June (Fig. 5f) but becomes more fully realized in July (Fig. 5g) when the SUC disappears. The strongest core of northeastward flow in the GW is located offshore of weaker northeastward flow in June–July since the center of the GW is actually situated just south of the transect (Fig. 5f and g see also Fig. 6c). Weaker inshore flow compared to the offshore flow was also noted in moored measurements located just north of our transect in Socotra Passage (Schott et al., 1997). The GW continues to develop, reaching a maximum in August–September with the strongest currents occurring in the northeastward branch of the coastal SC (Fig. 5h and i) as the GW moves northward (Jensen, 1991; Schott and McCreary, 2001; Vic et al., 2014; Wirth et al., 2002). The GW then gradually becomes weaker and

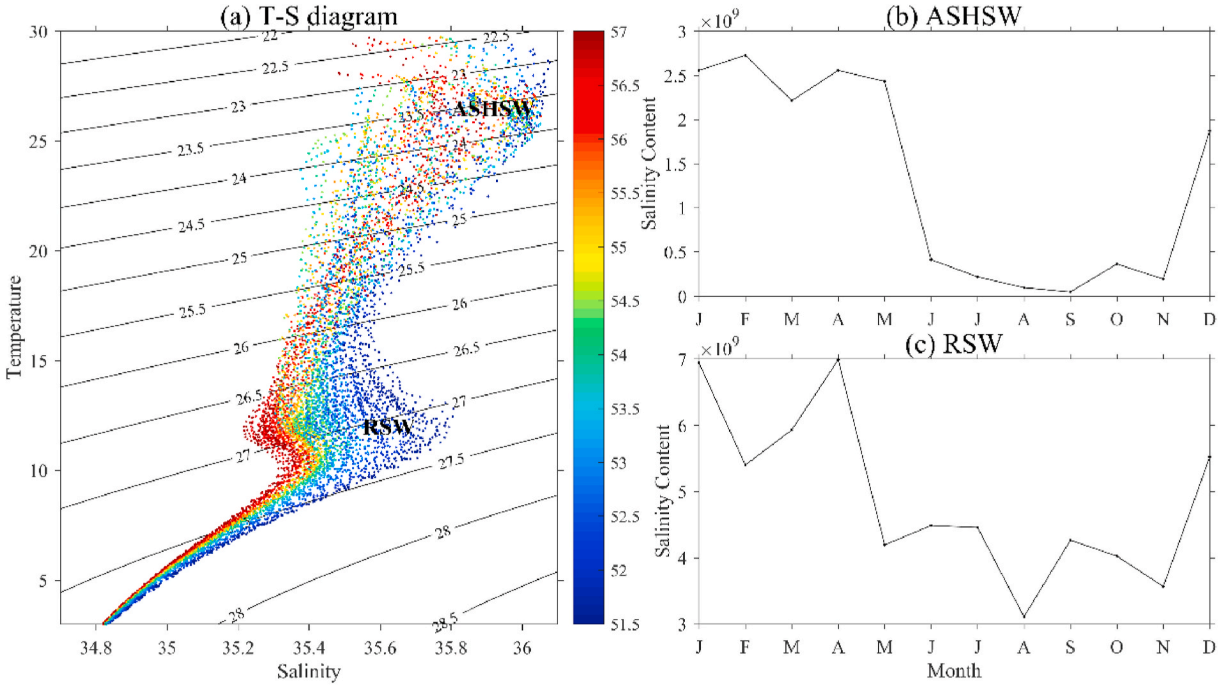

Fig. 4. **(a)** T-S diagram along the transect with contour lines of potential density (kg m^{-3}) and color-coded by longitude. T-S extrema indicate the Arabian Sea High Salinity Water (ASHSW) and Red Sea Water (RSW). The monthly salinity content (psu m^2) of **(b)** ASHSW and **(c)** RSW along the transect.

shoals with the arrival of upwelling Rossby waves (Vic et al., 2014), before moving further offshore from October to November (Fig. 5j and k). From September through November a subsurface southwestward flow returns again opposing the northeastward surface current (Fig. 5i–k). The core geostrophic velocity strengthens and shoals over that period from ~0.2 cm/s at ~1200 db (potential density of 27.6 kg m^{-3}) in September, to~ 1.7 cm/s at ~800 db (potential density of 27.3 kg m^{-3}) in October, and ~10.6 cm/s at ~300 db (potential density of 26.5 kg m^{-3}) depth in November (Fig. 5i–k).

To summarize, the plan mean geostrophic velocity on three isopycnal surfaces (potential densities of 24.5 kg m^{-3}, 26.5 kg m^{-3} and 27.5 kg m^{-3}) during the seasonal monsoon and transition periods are shown in Fig. 6. We also show the remotely sensed ADT in the upper panels. The 24.5 kg m^{-3} surface flow shows the monsoonal variation of the SC. In the period December–March the surface flow is mainly southwestward along the entire transect which is consistent with the ADT fields except for the northeastward flow nearest the shore (Fig. 6a). As noted above, this is suggestive of the bifurcation of the zonal flow near the shore into a northward branch supplying flow through the Socotra Passage (Kumar, 1999; Schott and Fisher, 2000). The flow on the 26.5 kg m^{-3} surface in December–March is strongly southwestward in-shore of 54°E and weak or reversing offshore (Fig. 6e). A similar flow pattern is observed on the 27.5 kg m^{-3} surface although the currents east of 54°E are completely reversed to the northeast (Fig. 6i). In April–June, the high ADT core near 7.5°N marks the spin-up of the GW. During April–June the SC surface flow (24.5 kg m^{-3} potential density) changes direction to be weakly northeastward and the subsurface flow is relatively weak although mainly southwestward at 26.5 kg m^{-3} and also at 27.5 kg m^{-3} farther offshore (Fig. 6b, f, j). The anticyclonic flow in the GW, that the altimetry data indicates is primarily south of our main transect line (Fig. 6c), is clearly evident in all three layers in July–August and has significantly strengthened (Fig. 6 c, g, k). In September–November, the center of the GW has weakened slightly and shifted northward and is still evident at the 24.5 kg m^{-3} and 26.5 kg m^{-3} surface, indeed with stronger offshore southeastward flow compared to July–August, but the flow on the deeper 27.5 kg m^{-3} surface is to the southwest west of ~53°E and weak along the rest of the transect (Fig. 6 d, h, l).

Guided by our results (Figs. 5 and 6), we choose the narrower longitude band of 51.5°E–54°E (cyan band in Fig. 6l) to produce the mean monthly geostrophic velocity profile over the annual cycle in the SC/SUC system (Fig. 7a). The primary geostrophic current above 1000 db from December to March is the southwestern current with a mean maximum core velocity of ~7.1 cm/s in March. From April to November, the northeastern surface current is strongly surface trapped in the upper ~400 db, attaining a maximum core velocity of 38.8 cm/s in September. Southwestern flow within the SUC is found at depth in April–May (2.2 cm/s at 200 dbar in May) and again from September through November (6.9 cm/s at 300 dbar in November) beneath the northeastward flow in the SC. The monthly volume transport integrated over the full depth (0–2000 db) has an annual cycle (Fig. 7b), with a maximum northeastward transport of 29.6 Sv in September largely reflecting the seasonality in the upper layer (Fig. 7a), and a maximum southwestward transport of 13 Sv in December corresponding to the stronger subsurface flow in the SUC (Fig. 7a). The annual mean volume transport of the full depth (0–2000 db) is 2.5 Sv.

4. Dynamics of the seasonal variability

The Indian Ocean circulation is largely controlled by the first and second baroclinic modes (Brandt et al., 2002; Beal and Donohue, 2013). Using altimeter data and a year-long mooring record, Brandt et al. (2002) found that the seasonal variations in the SSH of the central Arabian Sea can be mainly attributed to the westward propagation of the first and second baroclinic Rossby waves. In their study of the GW using altimeter data and two WOCE sections, Beal and Donohue (2013) found the initiation of the GW coincided with an influx of vorticity from the arrival of the annual first and second baroclinic Rossby waves from the eastern Arabian Sea that possibly influence the strength of the monsoon circulation in the SC region. Thus, the complicated vertical structure we observed in the SC/SUC system may encompass these first and second order modes or higher. To test this hypothesis, vertical normal mode decomposition, as outlined in Section 2, is performed on the mean geostrophic velocitybetween 51.5°-54°N. Significantly, the theoretical analysis presented here, employs a multi-decadal time series of

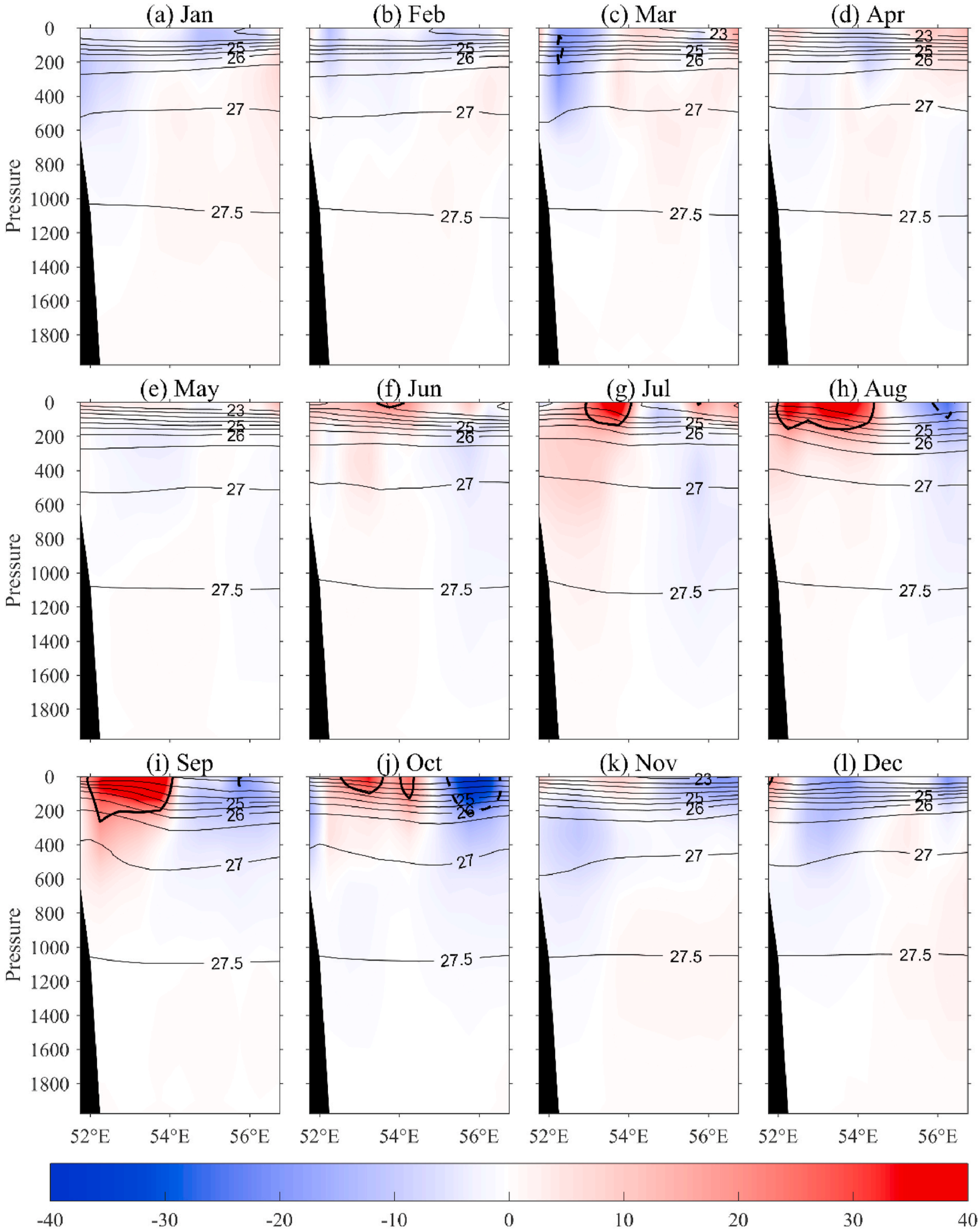

Fig. 5. Monthly geostrophic velocity (referenced to 2000 db, unit: cm/s) calculated using temperature and salinity shown in Figs. 2 and 3, respectively. The positive (negative) values represent northeastward (southwestward); thick black lines are 20 cm/s (solid) and −20 cm/s (dashed) velocity contours, the thin black lines are potential density isopycnals at 0.5 kg m^{-3} intervals.

subsurface measurements in the SC/SUC and is not conducted primarily relying on sea surface height data as undertaken by previous studies (Brandt et al., 2002; Beal and Donohue, 2013).

The sum of the barotropic mode and the first two baroclinic modes contributes 99.27% of the total seasonal variance of geostrophic velocity (Fig. 8f), and so simulates the observed velocity structure very well (Fig. 7a); the barotropic mode, the first and second baroclinic modes each contribute 23.3%, 63.2% and 12.8%, respectively. The barotropic and the first baroclinic mode each possess a strong seasonal cycle (Fig. 8a and b). As expected, the barotropic mode shows in-phase variations over the whole depth range (Fig. 8a), mostly reflecting the seasonal cycle of the surface SC which is forced by the monsoon wind (see

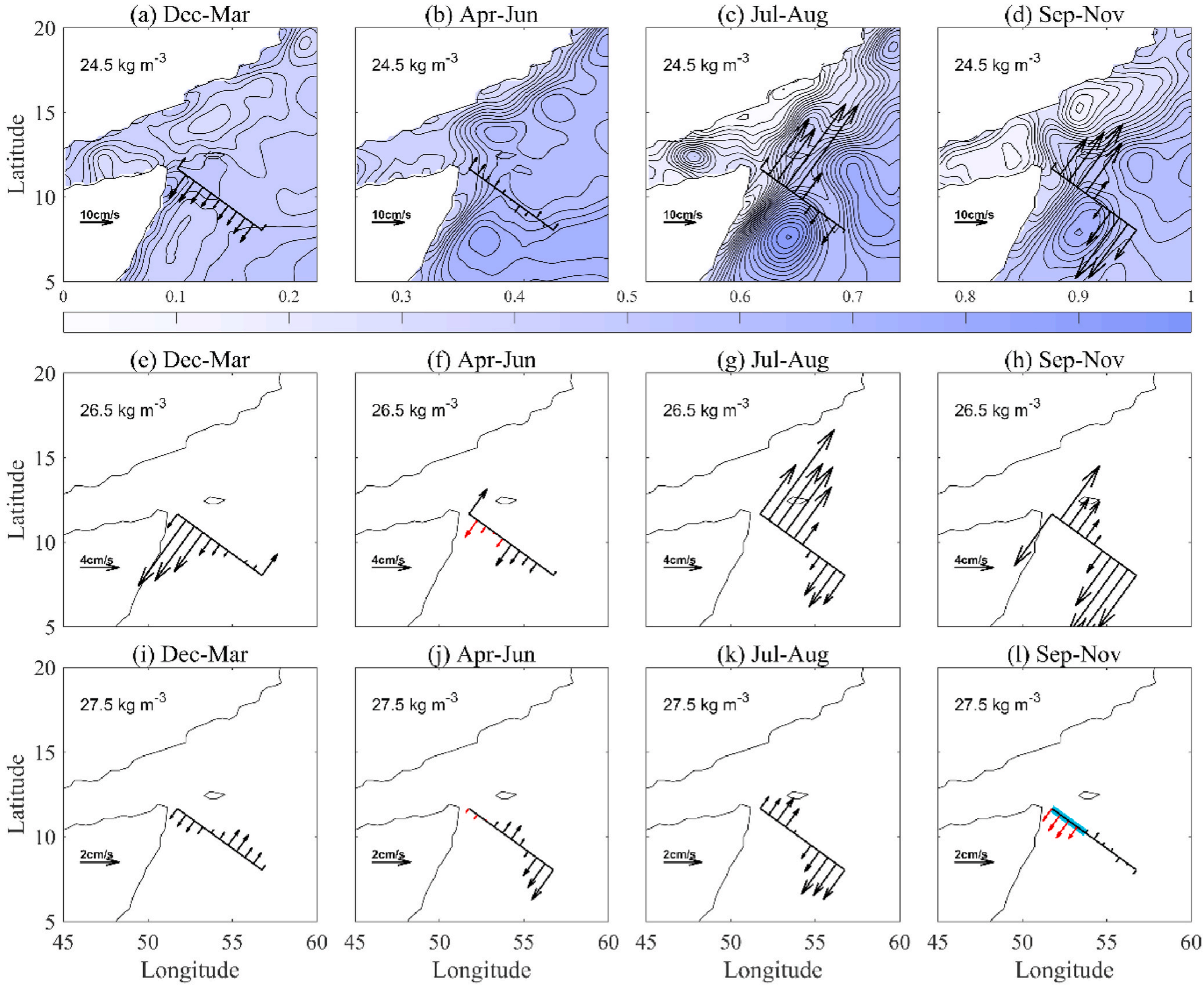

Fig. 6. Plan view of the mean geostrophic velocity (cm s^{-1}) on isopycnal surfaces of 24.5 kg m^{-3} (a–d), 26.5 kg m^{-3} (e–h) and 27.5 kg m^{-3} (i–l) in December–March (a,e,i), April–June (b,f,j), July–August (c,g,k) and September–November (d,h,l). The shading in (a–d) represents the remotely sensed absolute dynamic topography (m), the contour interval is 0.02 m. The red arrows represent where subsurface flows are opposite to the surface flows. The cyan band in (l) represents the area over which the mean geostrophic flow is calculated for Fig. 7a.

Figs. 7 and 9a). The first baroclinic mode exhibits opposing velocity above and below ~700 dbar (~27.2 kg m^{-3} potential density) (Fig. 8b). The first baroclinic mode is primarily related to the temperature structure (Fig. 9b), which is affected by the wind (Fig. 9a) and the arrival of the Rossby wave from the eastern Arabian Sea basin (Wang et al., 2018). The second baroclinic mode possesses a weaker annual variation (Fig. 8c) with the strongest currents evident in the surface layer during the fall transition of August–November. The second baroclinic mode shows consistent flow direction within three layers, separated at ~200 db (26 kg m^{-3} potential density) and ~1100 db (27.5 kg m^{-3} potential density). In this case, the stratification is clearly related to the salinity structure (Fig. 9c). Superimposition of the barotropic and the first baroclinic mode reproduces the surface current (Fig. 8d, combined 86.5% of the total variance), while the first and second baroclinic modes best represents the subsurface current above 1000 db (Fig. 8e, combined 75.9% of the total variance). Below 1000 db, the sum of both baroclinic modes and the barotropic mode is needed to correctly reproduce the currents (Fig. 8f), particularly in the boreal summer monsoon.

The seasonality of the SC/SUC is thus determined by the local baroclinic structure derived from the vertical temperature and salinity profiles. Subsurface undercurrents seasonally opposing the surface layer flow have been observed in other western boundary current systems, such as the Agulhas Current (Beal and Bryden, 1997; Donohue and Firing, 2000; Beal, 2009), the Gulf Stream (Richardson and Knauss, 1971; Richardson, 1977), the Mindanao Current (Ren et al., 2017; Hu et al., 2016; Wang et al., 2015; Zang et al., 2020), and the Kuroshio (Wang and Hu, 2012; Wang et al., 2014; Lien et al., 2015), that are largely driven by changes in the local wind stress and Rossby waves driven by the remote wind stress. However, the SC/SUC is also obviously dominated by high salinity water masses on seasonal time scales, with a salinity section characterized by a three-layer structure (Fig. 9b). The intrusion of a high salinity water mass will act to increase the dynamic height gradient across the transect (e.g. equation (3)). Hence we speculate that, in addition to the wind and Rossby waves, the seasonality of the high salinity water masses (ASHSW and RSW) will have an important effect on the seasonality of the SC/SUC structure. To test this, we removed the high salinity water masses of ASHSW and RSW above the 27.5 kg m^{-3} isopycnal surface by setting salinity greater than 35.5 to be 35.5 psμ and re-calculated the geostrophic velocity accordingly (Fig. 7c). In the salinity-adjusted geostrophic velocity, the southwestward flow in the upper 1000 db from November–June is stronger but the northeastward flow from June–October is weaker (Fig. 7c).

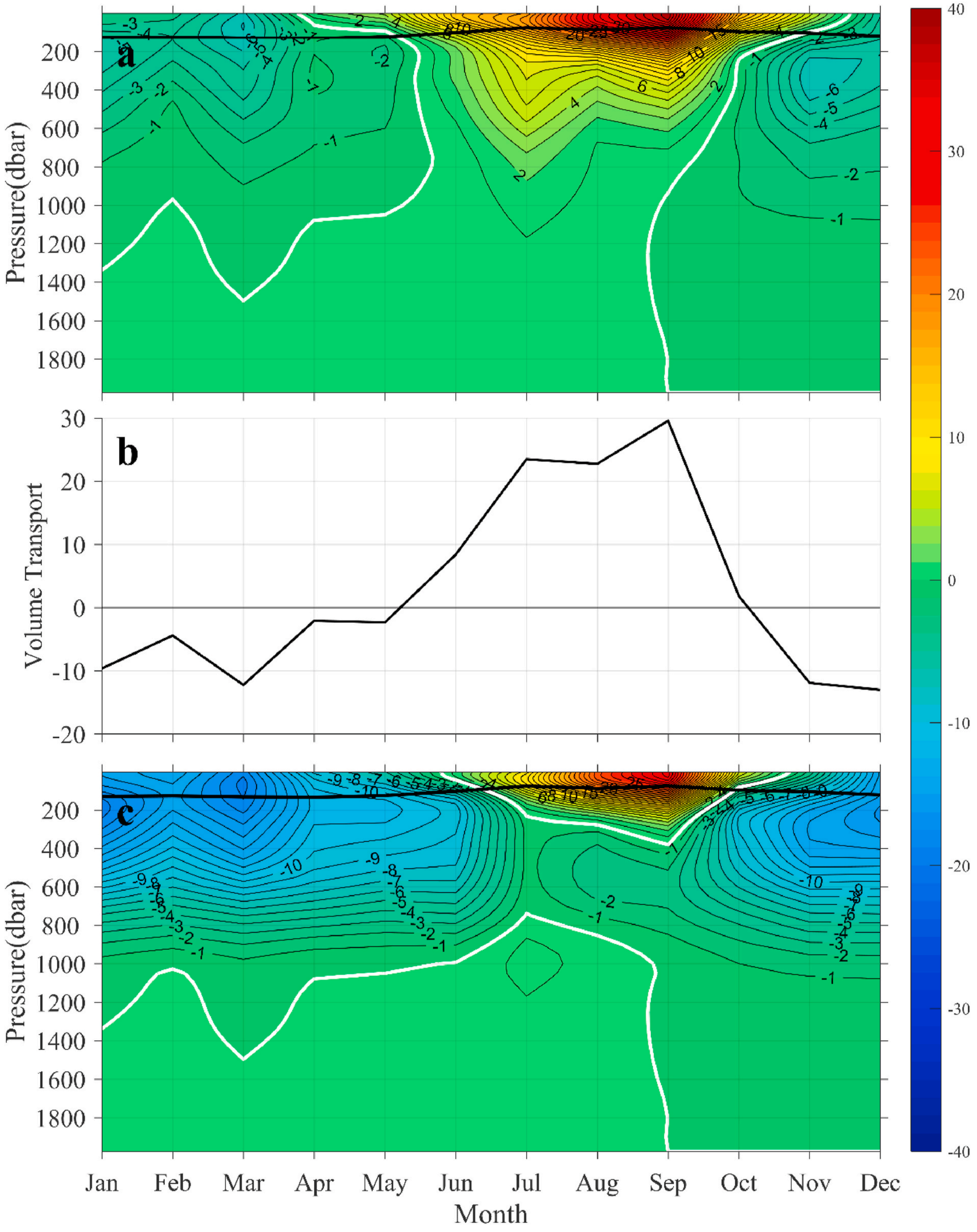

Fig. 7. (a) Monthly mean geostrophic velocity (cm/s) between 51.5 and 54°E; (b) Monthly volume transport (unit: Sv = 10^6 m^3/s) of the full depth (0–2000 db); (c) Monthly mean geostrophic velocity (cm/s) between 51.5 and 54°E, where the high salinity water >35.5 is set to be 35.5. In (a,c) the positive (negative) values represent northeastward (southwestward) flow, white lines are the zero velocity contours.

Furthermore, in the near-surface layer (upper 200 db) the northeastward flow begins later and reverses earlier and does not extend throughout the water column (Fig. 7c) as in the observed geostrophic flow (Fig. 7a). In fact, when the high RSW is removed, an opposing southwestward SUC appears in July–September to the SC (Fig. 7c), in contrast to that observed in the real system where both the surface and subsurface flows are northeastward (Fig. 7a). This supports our hypothesis that it is the presence of the high salinity water masses from the Northern Arabian Sea that influence the strength and direction of the currents in the SC/SUC system.

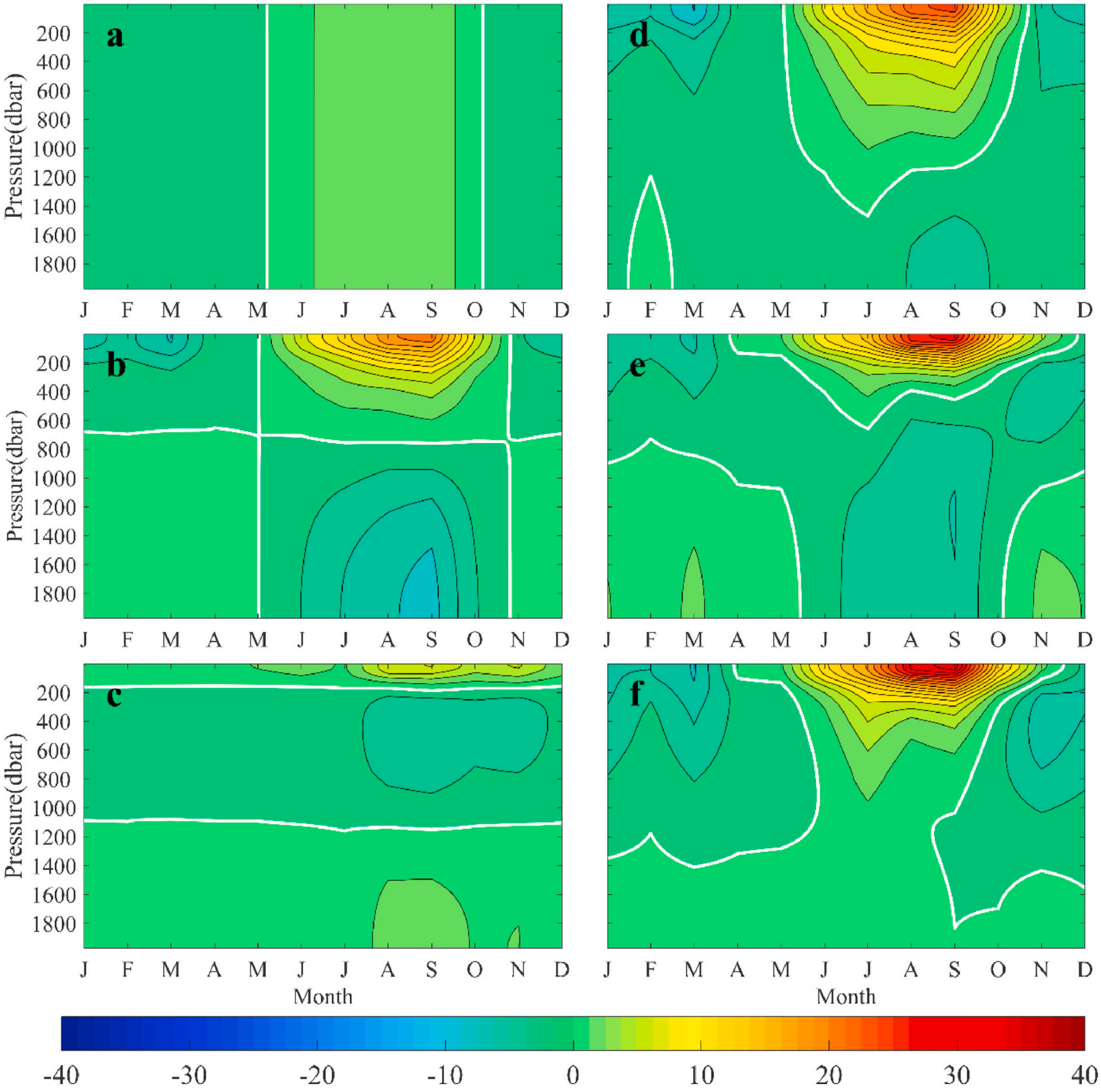

Fig. 8. Monthly mean geostrophic velocity (cm/s) between 51.5 and 54°E decomposed into (a) barotropic mode, (b) first baroclinic mode, (c) second baroclinic mode, (d) sum of the barotropic and the first baroclinic modes, (e) sum of the first and second baroclinic modes, (f) sum of the barotropic and the first two baroclinic modes. The white lines are the zero velocity contours.

5. Summary and conclusions

This study investigated the characteristics and dynamics of the seasonality of the SC/SUC system using a multi-decadal record constructed using XBT and Argo profile data. There is a monsoonal reversal of the SC, which is southwestward (northeastward) in the winter (summer) monsoon. Our observations of the seasonal phenology of the *surface* SC using a multi-decadal record are similar to that found in previous studies (Schott and McCreary, 2001; Beal et al., 2013; Jensen, 1991). However, our study provides new information on the observed seasonality of the *subsurface* SUC. The multi-year observational time series showed the southwestward SUC occurs in April–June and again from September–November, opposing the northeastward flow in the surface layer. During the boreal spring transition, the core of the undercurrent in April is located at ~500 db with a core geostrophic velocity of 2.5 cm/s that shoals to 200 db, and widens and strengthens to 4 cm/s in May (Fig. 5). Quadfasel and Schott (1983) observed an SUC at ~200 db depth from shipboard velocity profilers during a single May cruise with a much stronger core. During the boreal fall transition period, the core depth of the SUC shoals from 1200 db in September to 800 db in October and 300 db in November, with core speeds that strengthen from 0.2 cm/s to 1.7 cm/s to 10.6 cm/s, respectively in each successive month before quickly disappearing in December. In contrast, Schott and Fisher (2000) found the SUC present throughout the entire winter monsoon (November 1995–February 1996) based on an array of moored acoustic Doppler current profilers. Our multi-year near-repeat transect measurements enable us to resolve the seasonal cycle of SUC in more detail compared to those of previous studies. The surface flow largely controls the seasonal cycle in transport (Fig. 7b) with a northeastward 29.6 Sv maximum in the summer monsoon, while the stronger SUC in the fall transition results in a southwestward transport of 13.0 Sv.

The complicated vertical structure of the SC/SUC system indicates upper and lower current reversals that vary from month to month. Vertical mode decomposition found the barotropic and the first baroclinic modes both possess a strong seasonal cycle with the surface SC well represented by the combination of these two modes. The second

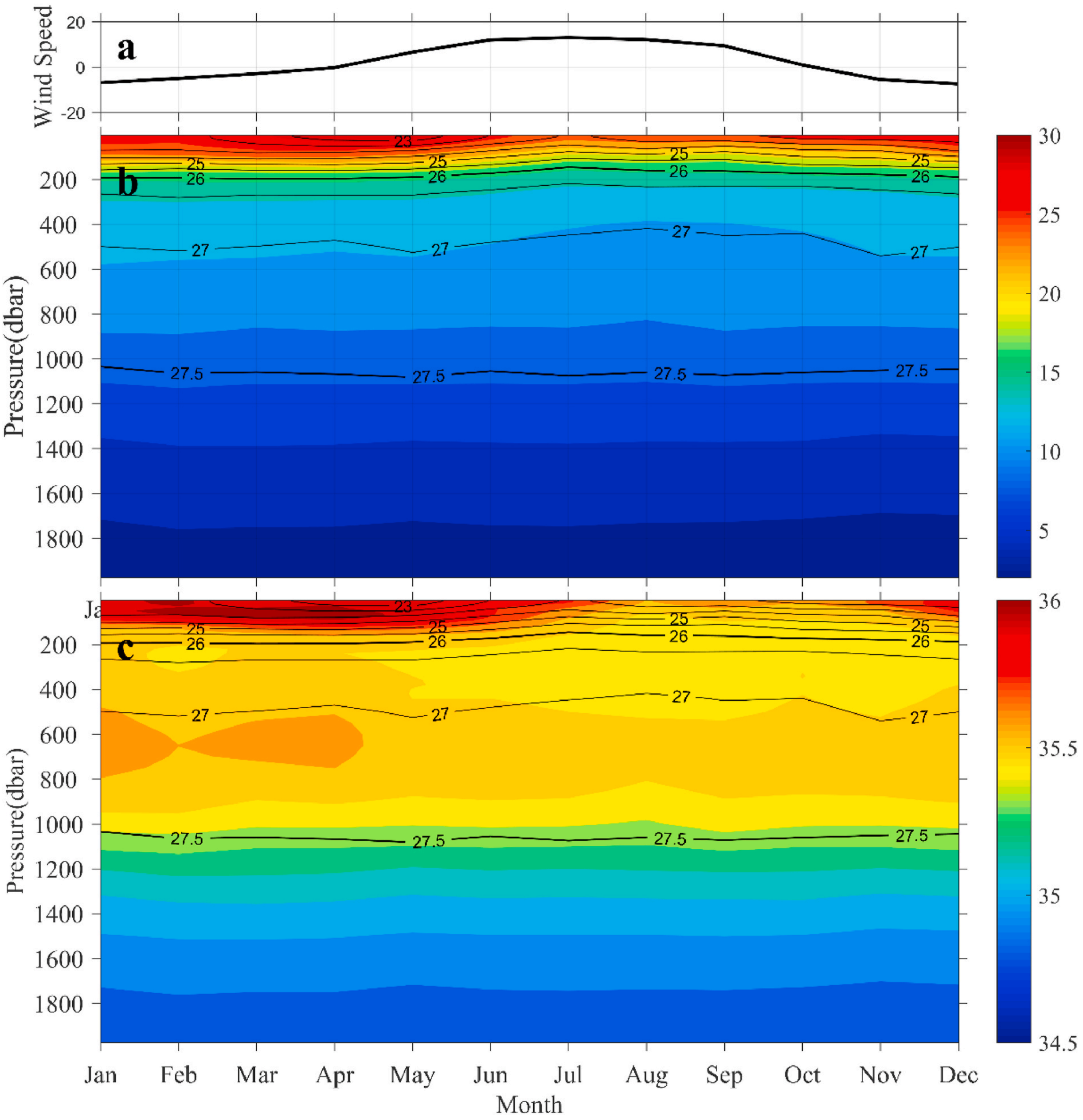

Fig. 9. Monthly mean (a) across-transect wind velocity (m/s), (b) temperature, and (c) salinity between 51.5 and 54°E. The positive (negative) values in (a) represent southwest (northeast) wind. The thin black lines in (b) and (c) are the potential density isopycnals at 0.5 kg m^{-3} intervals.

baroclinic mode possesses an annual variation and a three-layer structure more related to the salinity variations (Fig. 9b). The SUC variation in the upper 1000 db can be represented by the combination of the first and second baroclinic modes. Below 1000 db, the barotropic and perhaps also the second baroclinic mode is required to adequately reproduce the flow, particularly in July–September. This period coincides with the barotropic spin-up of the northern Somali Gyre (e.g. Jensen, 1991) as well as the strengthening of the GW (Fig. 5). It remains unclear how these circulation features may act to influence the deeper water column.

We found that the seasonality of the SUC is controlled not only by the baroclinic adjustment resulting from the onset of the monsoon wind as previously suggested by modelling studies (e.g. Jensen, 1991, 2001; McCreary and Kundu, 1988; McCreary et al., 1993), but also by the horizontal structure of salinity. Many local and remote forces can cause the horizontal variations of temperature and salinity, including the monsoonal circulation (Schott and McCreary, 2001), planetary waves (Rao et al., 2010) and water mass intrusions (Kumar and Prasad, 1999; Prasad and Ikeda, 2002). Specifically, we found that the presence of salty water masses from the northern Arabian Sea during the boreal summer monsoon prevents the formation of a southwestward flowing SUC and results in a baroclinic structure that supports a subsurface northeastward flow, aligned with the surface current. Thus, the high salinity water masses in both the surface layer (ASHSW) and subsurface layer (RSW) strengthen the northeastward flow throughout the upper 1000 m of the water column. This suggests that salinity dynamics play a fundamental role in the circulation of the boundary current system of the Arabian Sea. Nonetheless, it is worth noting that there are significantly less salinity profile data available compared to temperature profiles. This is particularly the case near to the Somali shoreline in depths shallower that 2000 db that are not sampled by Argo and hence the gridded Roemmich and Gilson (2009) climatology relies on the historically available data in those poorly sampled regions. Clearly simultaneous salinity, temperature and velocity profile measurements in the near-coastal region of Somalia are still needed.

In this paper, the seasonal cycle of SC/SUC system is based on high resolution data collected over multiple years but only along one transect that intersects the Arabian Sea WBC system. However, many observations and model studies have shown that the SC/SUC system at different latitudes are not necessarily in phase. The latitudinal differences in the SC/SUC system can be affected by both local and remote forcing mechanisms, such as monsoon winds, barotropic/baroclinic instability, and planetary waves (Quadfasel and Schott 1983; Schott et al., 1990; Fischer et al., 2002; Jensen, 1991; Vic et al., 2014; Wang et al., 2018). Some model simulations have provided a mechanistic analysis of the SC/SUC system (Jensen, 1991; Wirth et al., 2002; Vic et al., 2014; Wang et al., 2018). For example, Jensen (1991) found the early return of the southward undercurrent in the fall transition is likely caused by baroclinic instability of the GW. Wirth et al. (2002) suggested that the variability of circulation in the western Arabian Sea is not only due to the wind field, but that a substantial part is caused by the chaotic nature of the ocean dynamics. Wang et al. (2018) showed that both annual Rossby waves and nonlinear terms impact the SC variability. Sustained observations of this complicated system in the Arabian Sea, such as via the Argo network, glider surveys and repeat sampling along the XBT transect, are still needed to verify these model results, as recommended by the community in the recent Indian Ocean Observing System for the future (Beal et al., 2019).

Credit statement

Nan Zang: Formal Analysis, Investigation, Visualization, Writing.

Janet Sprintall: Conceptualization, Funding Acquisition, Supervision, Writing.

Rémi Ienny: Formal Analysis, Investigation, Visualization.

Fan Wang: Funding Acquisition, Supervision.

Declaration of competing interest

The authors declare that they have no known competing financial interests or personal relationships that could have appeared to influence the work reported in this paper.

Acknowledgements

We appreciate the comments from two anonymous reviewers and guest editor Dr. Jérôme Vialard that strengthened this manuscript. We thank the crews and ships that collected the IX-12 XBT data that was processed, managed and provided by Lisa Krummel (Bureau of Meteorology, Australia), Rebecca Cowley (CSIRO, Australia) and Ann Gronell (CSIRO, Australia). XBT data are available through http://imos.org.au/data/. Argo data are from the China Argo Real-time Data Center (http://www.argo.org.cn/). The gridded Argo salinity and temperature data are from the Scripps Institution of Oceanography optimally interpolated product (http://sio-argo.ucsd.edu/RG_Climatology.html). All Argo data were collected and made freely available by the International Argo Program and the national programs that contribute to it (http://www.argo.ucsd.edu, http://argo.jcommops.org). The Argo Program and the XBT program are part of the Global Ocean Observing System. The ADT product was obtained from the Archiving, Validation, and Interpretation of Satellite Oceanographic (AVISO; https://www.aviso.altimetry.fr). The wind velocity product is from the Cross-Calibrated Multi-Platform (CCMP) Level 3.5a (https://climatedataguide.ucar.edu/climate-data/ccmp-cross-calibrated-multi-platform-wind-vector-analysis). This work was supported by NOAA's Global Ocean Monitoring and Observing Program to JS (Award NA20OAR4320278); ONR project N00014-15-1-2313 to JS; National Key Research and Development Program (No. 2017YFA0603201) to NZ and FW, and The State Key Program of National Natural Science of China (No.41730534) to NZ and FW.

References

Bailey, R., Gronell, A., Phillips, H., Tanner, E., Meyers, G., 1994. Quality Control Cookbook for XBT Data (Expendable Bathythermograph Data). CSIRO, Australia, p. 37 (CSIRO Marine Laboratories Reports: 221).

Beal, L.M., Bryden, H.L., 1997. Observation of an Agulhas undercurrent. Deep-Sea Res. I 44, 1715–1724. https://doi.org/10.1016/S0967-0637(97)00033-2.

Beal, L.M., 2009. A time series of Agulhas Undercurrent transport. J. Phys. Oceanogr. 39, 2436–2450. https://doi.org/10.1175/2009JPO4195.1.

Beal, L.M., Hormann, V., Lumpkin, R., Foltz, G.R., 2013. The response of the surface circulation of the Arabian Sea to monsoonal forcing. J. Phys. Oceanogr. 43, 2008–2022. https://doi.org/10.1175/JPO-D-13- 033.1.

Beal, L.M., Ffield, A., Gordon, A.L., 2000. Spreading of Red Sea overflow waters in the Indian ocean. J. Geophys. Res. 105 (C4), 8549–8564. https://doi.org/10.1029/1999JC900306.

Beal, L.M., Donohue, K.A., 2013. The Great Whirl: observations of its seasonal development and interannual variability. J. Geophys. Res. 118, 1–13. https://doi.org/10.1029/2012JC00819.

Beal, L.M., Chereskin, T.K., 2003. The volume transport of the Somali Current during the 1995 southwest monsoon. Deep-Sea Res. II 50, 2077–2089. https://doi.org/10.1016/S0967-0645(03)00046-8.

Beal, L.M., Vialard, J., Roxy, M.K., lead authors, 2019. Full Report. IndOOS-2: A Roadmap to Sustained Observations of the Indian Ocean for 2020-2030. CLIVAR-4/2019, p. 206. https://doi.org/10.36071/clivar.rp.4.2019. GOOS-237.

Brandt, P., Dengler, M., Rubino, A., Quadfasel, D., Schott, F., 2002. Intraseasonal variability in the southwestern Arabian Sea and its relation to the seasonal circulation. Deep-Sea Res. II 50, 2129–2141. https://doi.org/10.1016/S0967-0645(03)00049-3.

Cane, M., Gent, P., 1984. Reflections of low-frequency equatorial waves at arbitrary western boundaries. J. Mar. Res. 42, 487–502.

Donguy, J.-R. and G. Meyers, Observations of geostrophic transport variability in the western tropical Indian Ocean, Deep-sea Res., 42(6), https://doi.org/10.1016/0967-0637(95)00047-A.

Donohue, K.A., Firing, E., 2000. Comparison of three velocity sections of the Agulhas current and Agulhas undercurrent. J. Geophys. Res. 105 (C12), 28,585–28,593. https://doi.org/10.1029/1999JC000201.

Fischer, A.S., Weller, R.A., Ridnich, D.L., et al., 2002. Mesoscale eddies, coastal upwelling, and the upper-ocean heat budget in the Arabian Sea. Deep-Sea Res. 49 (12), 2231–2264. https://doi.org/10.1016/S0967-0645(02)00036-X.

Hanawa, K., Rual, P., Bailey, R., Sy, A., Szabados, M., 1995. A new depth-time equation for Sippican or TSK T-7, T-6 and T-4 expendable bathythermographs (XBT). *Deep-Sea Res.* Part I 42 (8), 1423–1451. https://doi.org/10.1016/0967-0637(95)97154-Z.

Hastenrath, S., Greischar, L., 1991. The Monsoonal current regimes of the tropical Indian Ocean: observed surface flow fields and their geostrophic and wind-driven components. J. Geophys. Res. 96 (C7), 12619–12633. https://doi.org/10.1029/91JC00997.

Hu, S.J., Hu, D.X., Guan, C., et al., 2016. Interannual variability of the Mindanao current/undercurrent in the direct observations and numerical simulations. J. Phys. Oceanogr. 46, 483–499. https://doi.org/10.1175/JPO-D-15-0092.1.

Jensen, T.G., 1991. Modeling the seasonal undercurrents in the Somali Current system. J. Geophys. Res. 96 (C12), 22151–22167. https://doi.org/10.1029/91JC02383.

Jensen, T.G., 2001. Application of the GWR method to the tropical Indian ocean. Mon. Weather Rev. 129, 470–485. https://doi.org/10.1175/1520-0493(2001)129<0470:AOTGMT>2.0.CO;2.

Joseph, S., Freeland, H.J., 2005. Salinity variability in the Arabian Sea. Geophys. Res. Lett. 32, L09607. https://doi.org/10.1029/2005GL022972.

Kumar, S. Prasanna, Prasad, T.G., 1999. Formation and spreading of Arabian Sea high-salinity water mass. J. Geophys. Res. 104 (C1), 1455–1464. https://doi.org/10.1029/1998JC900022.

Lien, R.C., Ma, B., Lee, C.M., et al., 2015. The Kuroshio and luzon undercurrent east of luzon island. Oceanography 28 (4), 54–63. https://doi.org/10.5670/oceanog.2015.81.

Lighthill, M.J., 1969. Dynamic response of the Indian ocean to onset of the southwest monsoon. Phil. Trans. Roy. Soc. Lond. 265 (1159), 45–92.

Luther, M.E., 1999. Interannual variability in the Somali current 1954-1976. Nonlinear Anal. Theor. Methods Appl. 35, 59–83. https://doi.org/10.1016/S0362-546X(98)00098-4.

McCreary, J.P., Kundu, P.K., 1985. Western boundary circulation driven by an alongshore wind: with application to the Somali Current system. J. Mar. Res. 43, 493–516.

McCreary, J.P., Kundu, P.K., 1988. A numerical investigation of the Somali current during the southwest monsoon. J. Mar. Res. 46, 25–58. https://doi.org/10.1357/002224088785113711.

McCreary, J.P., Kundu, P.K., Molinari, R.L., 1993. A numerical investigation of dynamics, thermodynamics and mixed-layer processes in the Indian Ocean. Prog. Oceanogr. 31, 181–244. https://doi.org/10.1016/0079-6611(93)90002-U.

Murray, S.P., Johns, W., 1997. Direct observations of seasonal exchange through the Bab el Mandab Strait. Geophys. Res. Lett. 24 (21), 2557–2560. https://doi.org/10.1029/97GL02741.

Philander, G., Pacanowski, R.C., 1981. The oceanic response to cross-equatorial winds (with application to coastal upwelling in low latitudes). Tellus 33, 201–210.

Prasad, T.G., Ikeda, M., Kumar, S.P., 2001. Seasonal spreading of the Persian Gulf water mass in the Arabian Sea. J. Geophys. Res. 106 (C8), 17059–17071. https://doi.org/10.1029/2000JC000480.

Prasad, T.G., Ikeda, M., 2002. A numerical study of the seasonal variability of Arabian Sea high-salinity water. J. Geophys. Res. 107 (C11), 3197. https://doi.org/10.1029/2001JC001139.

Quadfasel, D.R., Schott, F., 1983. Southward subsurface flow below the Somali Current. J. Geophys. Res. 88 (C10), 5973–5979. https://doi.org/10.1029/JC088iC10p05973.

Rao, R.R., Girish Kumar, M.S., Ravichandran, M., Rao, A.R., Gopalakrishna, V.V., Thadathil, P., 2010. Interannual variability of Kelvin wave propagation in the wave guides of the equatorial Indian Ocean, the coastal Bay of Bengal and the southeastern Arabian Sea during 1993–2006. Deep Sea Res. Part I 57 (1), 1–13. https://doi.org/10.1016/j.dsr.2009.10.008.

Ren, Q.P., Li, Y.L., Wang, F., et al., 2017. Seasonality of the Mindanao current/undercurrent systerm. J. Geophys. Res. 123, 1105–1122. https://doi.org/10.1002/2017JC013474.

Reppin, J., Schott, F.A., Fischer, J., Quadfasel, D., 1999. Equatorial currents and transports in the upper central Indian Ocean: annual cycle and interannual variability. J. Geophys. Res. 104 (C7), 15495–15514. https://doi.org/10.1029/1999JC900093.

Richardson, P.L., Knauss, J.A., 1971. Gulf Stream and western boundary undercurrent observations at cape hatteras. Deep-Sea Res. 18, 1089–1109. https://doi.org/10.1016/0011-7471(71)90095-7.

Richardson, P.L., 1977. On the crossover between the Gulf Stream and the western boundary undercurrent. Deep-Sea Res. 24, 139–159. https://doi.org/10.1016/0146-6291(77)90549-5.

Roemmich, D., Gilson, J., 2009. The 2004-2008 mean and annual cycle of temperature, salinity, and steric height in the global ocean from the Argo Program. Prog. Oceanogr. 82, 81–100.

Schott, F.A., Swallow, J.C., Fieux, M., 1990. The Somali Current at the equator: annual cycle of currents and transports in the upper 1000m and connection to neighbouring latitudes. Deep-Sea Res. 37 (12), 1825–1848. https://doi.org/10.1016/0198-0149(90)90080-F.

Schott, F., Fischer, J., Garternicht, U., Quadfasel, D., 1997. Summer monsoon response of the northern Somali current, 1995. Geophys. Res. Lett. 24, 2565–2568.

Schott, F.A., Fisher, J., 2000. Winter monsoon circulation of the northern Arabian Sea and Somali current. J. Geophys. Res. 105 (C3), 6359–6376. https://doi.org/10.1029/1999JC900312.

Schott, F.A., McCreary, J.P., 2001. The monsoon circulation of the Indian Ocean. Prog. Oceanogr. 51 (1), 1–123. https://doi.org/10.1016/S0079-6611(01)00083-0.

Schott, F.A., Xie, S.P., McCreary, J.P., 2009. Indian Ocean circulation and climate variability. Rev. Geophys. 47 (1), RG1002. https://doi.org/10.1029/2007RG000245.

Shapiro, G.I., Meschanov, S.L., 1991. Distribution and spreading of Red Sea Water and salt lens formation in the northwest Indian Ocean. Deep-Sea Res. Part A 38 (1), 21–34. https://doi.org/10.1016/0198-0149(91)90052-H.

Thompson, Emery, 2014. Data Analysis Methods in Physical Oceanography, third ed. Elsevier Science, p. 728.

Vic, C., G, Roullet, X., Carton, Capet, X., 2014. Mesoscale dynamics in the Arabian Sea and a focus on the Great Whirl lifecycle: a numerical investigation using ROMS. J. Geophys. Res. 119 (9), 6422–6443.

Visbeck, M., Schott, F., 1992. Analysis of seasonal current variations in the western equatorial Indian Ocean: direct measurements and a GFDL model comparison. J. Phys. Oceanogr. 22, 1112–1128. https://doi.org/10.1175/1520-0485(1992)022<1112:AOSCVI>2.0.CO;2.

Wang, F., Zang, N., Li, Y.L., Hu, D., 2015. On the subsurface countercurrents in the Philippine Sea. J. Geophys. Res. 120, 131–144. https://doi.org/10.1002/2013JC009690.

Wang, H., McClean, J.L., Talley, L.D., Yeager, S., 2018. Seasonal cycle and annual reversal of the Somali Current in an eddy-resolving global ocean model. J. Geophys. Res. 123 (9), 6562–6580. https://doi.org/10.1029/2018jc013975.

Wang, Q.Y., Hu, D.X., 2012. Origin of the luzon undercurrent. Bull. Mar. Sci. 88 (1), 51–60. https://doi.org/10.5343/bms.2011.1020.

Wang, Q.Y., Zhai, F.G., Hu, D.X., 2014. Variations of Luzon Undercurrent from observations and numerical model simulaitons. J. Geophys. Res. 119, 3792–3805. https://doi.org/10.1002/2013JC009694.

Wijffels, S.E., Willis, J., Domingues, C.M., Barker, P., White, N.J., Gronell, A., Ridgway, K., Church, J.A., 2008. Changing Expendable Bathythermograph fall rates and their impact on estimates of thermosteric sea level rise. J. Clim. 21, 5657–5672. https://doi.org/10.1175/2008JCLI2290.1.

Wirth, A., Willebrand, J., Schott, F., 2002. Variability of the Great Whirl from observations and models. Deep-Sea Res. II 49, 1279–1295. https://doi.org/10.1016/S0967-0645(01)00165-5.

Zang, N., Wang, F., Sprintall, J., 2020. The intermediate water in the Philippines sea. J. Oceanol. Limnol. https://doi.org/10.1007/s00343-020-0035-4.